

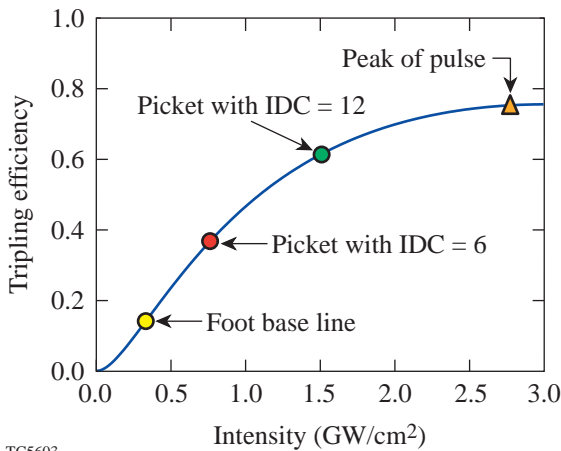
The Smoothing Performance of Ultrafast Pickets on the NIF

Introduction

In the direct-drive approach to inertial confinement fusion (ICF), the focal spots of a symmetrically arranged cluster of high-intensity, ultraviolet (UV) laser beams directly irradiate a capsule.^{1,2} The base-line design for a direct-drive ignition target on the National Ignition Facility (NIF) uses shock preheat to control the isentrope of the ablation surface and the fuel. Control of the isentrope α (where α is the ratio of the fuel pressure to the Fermi-degenerate pressure) is achieved by changing the laser pulse shape. The UV pulse shape corresponding to $\alpha = 3$ is chosen for the base-line design. This shape can be logically divided into two regions: a low-intensity “foot” (of duration ~ 4.2 ns) followed by a high-intensity “drive” (duration ~ 5 ns). This pulse shape represents a compromise that provides a certain safety margin for the implosion by reducing the target’s sensitivity to laser nonuniformity by ensuring that the target will remain intact during the drive portion of the pulse; however, laser nonuniformity still re-

mains an important issue. The laser irradiation nonuniformity seeds the Rayleigh–Taylor hydrodynamic instability, which consequently degrades target performance.^{3,4}

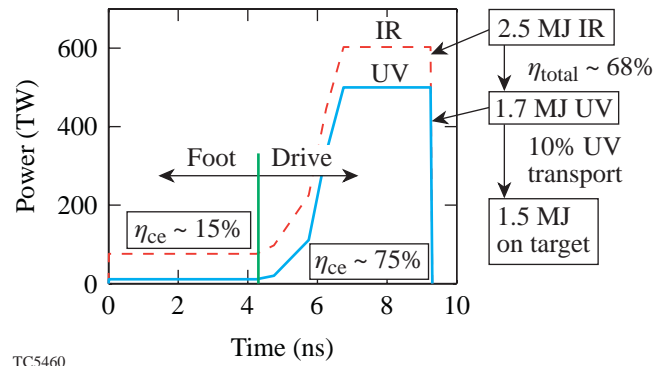
The energy efficiency of the KDP frequency-conversion crystals used in ICF lasers is a function of input intensity; efficiency increases as the third power of input intensity increases until saturation occurs (see Fig. 86.37). Consequently, the low-intensity foot portion of the pulse converts inefficiently and can represent a substantial overall reduction in the laser’s energy efficiency. As shown in Fig. 86.38, an $\alpha = 3$, direct-drive pulse has a total infrared (IR) energy of 2.5 MJ and a total UV energy delivered to target of 1.5 MJ (including 10% UV transport losses). The frequency-conversion efficiency in the foot of the $\alpha = 3$ pulse is $\sim 15\%$ and $\sim 75\%$ in the drive portion, yielding an overall efficiency of $\sim 68\%$. This issue is even more problematic for the indirect-drive approach, where the overall conversion efficiency is as low as



TC5603

Figure 86.37

The IR to UV frequency-conversion-efficiency curve for the NIF. The drive portions of an $\alpha = 3$ ICF pulse converts at efficiencies around 75%, where the efficiency is in saturation. The foot portion of the ICF pulse converts at a low efficiency of 15%. In addition, the frequency-conversion efficiency exhibits a third-power dependence for low-IR input intensity. This exacerbates any beam-to-beam power imbalance during the foot portion of an $\alpha = 3$ ICF pulse.



TC5460

Figure 86.38

The $\alpha = 3$, direct-drive ICF pulse, which is logically divided into two regions: a low-intensity “foot” (about 4.2 ns) followed by a high-intensity “drive” (about 5 ns). The IR power as a function of time (dashed line) required to produce the desired UV power onto target (solid line). The total IR energy is 2.5 MJ, and the total UV energy delivered to target (accounting for 10% UV transport losses) is 1.5 MJ. The frequency-conversion efficiency is $\sim 15\%$ in the foot and $\sim 75\%$ in the drive, which yields an overall efficiency of $\sim 68\%$.

50% due to a much longer low-intensity foot.⁵ Beam-to-beam power imbalance is also exacerbated for the low-intensity foot because of the third-power dependence of conversion efficiency on intensity at low intensities; during the drive portion of the ICF pulse the conversion efficiency is in saturation at $\sim 75\%$ and does not contribute significantly to beam-to-beam power imbalance.

Ultrafast picket-fence pulses were proposed by Rothenberg⁵ as a way to maximize conversion efficiency and minimize beam-to-beam power imbalance. In this article, we consider the application of the ultrafast pickets only to the foot portion of the $\alpha = 3$ pulse. We assume that the pickets are temporally blended into the drive portion of the pulse. Ultrafast pickets consist of a train of laser pulses with an inverse duty cycle (IDC), which is defined as the ratio of the pulse-repetition period to the pulse width, chosen to maintain near-constant target illumination and a peak intensity that delivers the same average power to the target as when picket-fence modulation is absent. For example, if a pulse train of 20-ps pulses with $\text{IDC} = 6$ is applied to the foot, the peak intensity of each picket can be increased sixfold while maintaining the same average power on target. Increasing the peak intensity sixfold boosts the conversion efficiency of the foot from 15% to 39% and the overall efficiency from 68% to 73% (see Fig. 86.39). (For indirect drive the overall conversion efficiency can be increased from $\sim 50\%$ to $\sim 72\%$ by using ultrafast pickets.⁵) For a pulse train of 10-ps pulse with $\text{IDC} = 12$, the efficiency of the foot is increased to 51% with an overall efficiency of 74%. The benefit of this shorter pulse is the minimized affect on beam-to-beam power imbalance as seen in Fig. 86.37.

The goal of this investigation is to assess the impact and benefits of implementing ultrafast pickets for direct-drive capsules on the NIF. The smoothing performance (defined as the time-integrated laser nonuniformity as a function of time) is the metric used to compare the ultrafast-picket-fence scheme to that of base-line 2-D SSD on the NIF. Various beam-smoothing techniques to be employed on the NIF are similar to those employed on the OMEGA^{6,7} laser to improve on-target laser uniformity, which reduces laser imprint. These techniques include two-dimensional smoothing by spectral dispersion (2-D SSD),^{8–10} distributed phase plates (DPP's),^{11,12} polarization smoothing,^{6,13,14} and multiple-beam overlap.

The code *Waaikwa*'¹⁵ is used to calculate the time evolution of the far field and the single-beam time-integrated laser nonuniformity for the first 3 ns of the foot. *Waaikwa*' will be

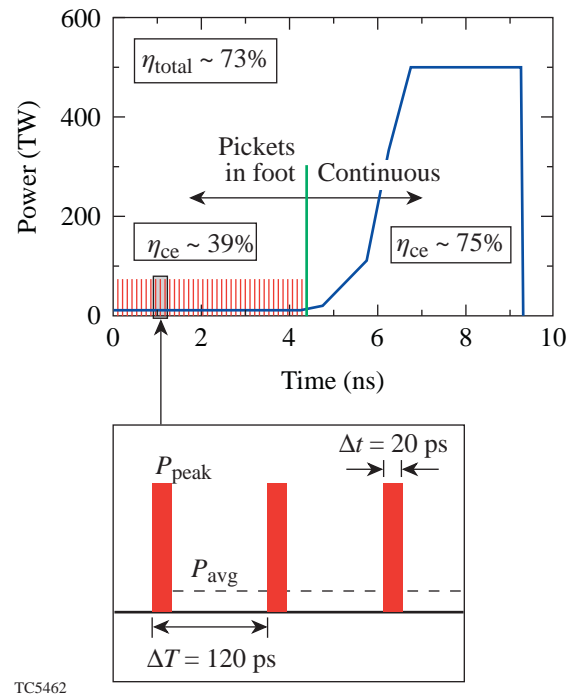


Figure 86.39

The UV power of an $\alpha = 3$, direct-drive pulse with ultrafast pickets applied during the foot. The frequency-conversion efficiency has been increased in the foot from 15% to $\sim 39\%$, which yields an overall efficiency of $\sim 73\%$.

used under a variety of near-field conditions that describe the base-line 2-D SSD system as well as various ultrafast-picket configurations. The calculated single-beam, time-dependent, laser nonuniformity will be used as the basis of comparison.

In the following sections we describe the base-line 2-D SSD system, the generation of an ultrafast picket pulse train, the far-field characteristics of ultrafast pickets, the smoothing performance, and conclusions.

Base-Line 2-D SSD

The 2-D SSD system on the NIF is similar to that on OMEGA with one exception: only one grating is used in the first SSD dimension on the NIF because it is implemented with a fiber-optic-based phase modulator. As a result, the beam suffers a residual time shear. OMEGA utilizes a bulk phase modulator in the first dimension so it can precompensate for this shear (compare Ref. 16). The second SSD dimension on the NIF has two gratings, like OMEGA. A schematic of the NIF's 2-D SSD design is shown in Fig. 86.40.

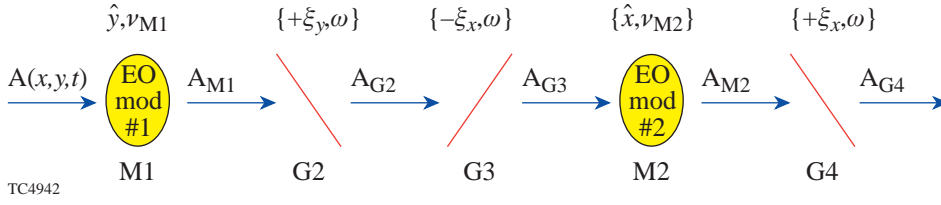


Figure 86.40

A schematic representation of the NIF's 2-D SSD system. Notice that the first dimension has only one grating, which causes a residual temporal shear across the beam.

The spatiotemporal evolution the complex-valued UV electric field of a 2-D SSD pulsed beam can be expressed as

$$E(x, y, t) \equiv E_0(x, y, t) e^{i\phi_{2\text{-D SSD}}(x, y, t)} e^{i\phi_{\text{DPP}}(x, y)}, \quad (1)$$

where $E_0(x, y, t)$ defines the electric field's pulse and beam shape, $\phi_{2\text{-D SSD}}$ is the 2-D SSD phase contribution, and $\phi_{\text{DPP}}(x, y)$ is the static DPP phase contribution. The mapping of the DPP phase contribution was designed to yield a far-field intensity distribution of an eighth-order super-Gaussian with a 95% enclosed energy contour of 3.40-mm diameter in the target plane. For these simulations, the fundamental spatial and temporal shapes of the pulsed beam are assumed to be separable prior to the 2-D SSD operation. The uncompensated grating operation distorts this fundamental shape and can be written as

$$E_0(x, y, t) \equiv G\{\text{beam}(x, y) \cdot \text{pulse}(t)\}, \quad (2)$$

where $\text{beam}(x, y)$ is the near-field beam shape, $\text{pulse}(t)$ is the temporal pulse shape, and $G\{\bullet\}$ represents an uncompensated grating operator, which is defined by

$$G\{f(x, y, t)\} \equiv f(x, y, \zeta), \quad (3)$$

where the spatially coupled time domain is given by $\zeta \equiv t - \xi_y y$ and ξ_y is the angular grating dispersion (see Ref. 16 for a detailed examination of the angular spectrum representation of the 2-D SSD operation). As a consequence of the assumed separability, the uncompensated grating operation couples the temporal pulse shape to the spatial dimension corresponding to the first SSD dimension while the spatial beam shape remains unaltered and is given by

$$E_0(x, y, t) \equiv \text{beam}(x, y) \cdot \text{pulse}(t - \xi_y y). \quad (4)$$

For the *Waasikwa*' simulations the fundamental beam shape at the final magnification is defined as a square-shaped 20th-order super-Gaussian:

$$\begin{aligned} \text{beam}(x, y) \equiv & \exp\left[-\ln(2)\left(\frac{|x|}{30.8 \text{ cm}}\right)^{20}\right] \\ & \times \exp\left[-\ln(2)\left(\frac{|y|}{30.8 \text{ cm}}\right)^{20}\right], \quad (5) \end{aligned}$$

which has an intensity full-width half-maximum (FWHM) width in each direction of $D_{\text{FWHM}} = 30.8 \text{ cm}$ and a 95% enclosed energy contour with a width in each direction of $D_{\text{NIF}} = 35.1 \text{ cm}$, and the fundamental pulse shape is given by a fourth-order super-Gaussian to a "flat-top":

$$\text{pulse}(t) \equiv \begin{cases} \exp\left[-\ln(2)\left(\frac{t-t_0}{19 \text{ ps}}\right)^4\right]; & 0 < t \leq t_{\text{peak}} \\ 1 & ; t > t_{\text{peak}} \end{cases}, \quad (6)$$

where the quantity t_0 is defined to yield a nominally, small initial value for the pulse, e.g., $\text{pulse}(0) = 0.001$, and the quantity t_{peak} defines the time when the pulse shape achieves a value of unity, i.e., $\text{pulse}(t_{\text{peak}}) = 1$. The foot pulse is defined in this manner to make a more accurate comparison of the early development of the nonuniformity with the ultrafast pickets defined later.

The spatially and temporally varying phase due to 2-D SSD is given by (see Ref. 16)

$$\begin{aligned} \phi_{2\text{-D SSD}}(x, y, t) \equiv & 3\delta_{\text{M1}} \sin[\omega_{\text{M1}}(t + \xi_y y)] \\ & + 3\delta_{\text{M2}} \sin[\omega_{\text{M2}}(t + \xi_x x)], \quad (7) \end{aligned}$$

where δ_{M1} is the first-dimension modulation depth, $\nu_{M1} \equiv \omega_{M1}/(2\pi)$ is the first-dimension microwave or radio frequency (RF) modulation frequency, ξ_y is the first-dimension angular grating dispersion, δ_{M2} is the second-dimension modulation depth, $\nu_{M2} \equiv \omega_{M2}/(2\pi)$ is the second-dimension RF modulation frequency, and ξ_x is the second-dimension angular grating dispersion. The factor of 3 in Eq. (7) indicates that the electric field has undergone frequency tripling from the IR to UV. The relevant NIF 2-D SSD base-line system parameters are assumed to be $\delta_{M1} = 16.7$, $\nu_{M1} = 8.76$ GHz, $\xi_y = 0.325$ ns/m, $\Delta\lambda_{M1} = 10.8$ Å, $\delta_{M2} = 8.37$, $\nu_{M2} = 3.23$ GHz, $\xi_x = 0.878$ ns/m, and $\Delta\lambda_{M2} = 2.0$ Å, assuming a nominal beam diameter of $D_{NIF} = 35.1$ cm.

The base-line 2-D SSD design for direct-drive NIF is defined in this article as having IR bandwidths of

$$\Delta\lambda_{M1} = 2\delta_{M1}\nu_{M1}\lambda_{IR}^2/c = 10.8 \text{ \AA}$$

and

$$\Delta\lambda_{M2} = 2\delta_{M2}\nu_{M2}\lambda_{IR}^2/c = 2.0 \text{ \AA}$$

in the first and second dimensions, respectively, where c is the vacuum speed of light and $\lambda_{IR} = 1053$ nm is the IR wavelength. Two different measures of combined UV bandwidth or widths of the temporal power spectrum are used here: the first measure is the root-sum-square and is defined by

$$\Delta\nu_{\text{rss}} = \sqrt{\Delta\nu_{M1}^2 + \Delta\nu_{M2}^2}, \quad (8)$$

where the UV bandwidths of each modulator are given separately by $\Delta\nu_{M1} \equiv 6\delta_{M1}\nu_{M1}$ and $\Delta\nu_{M2} \equiv 6\delta_{M2}\nu_{M2}$; and the second measure is known as the autocorrelation width¹⁷ and is defined by

$$\Delta\nu_{\text{eff}} = \frac{\left| \int \tilde{I}(\nu) d\nu \right|^2}{\int \tilde{I}(\nu)^2 d\nu}, \quad (9)$$

where the quantity $\tilde{I}(\nu) \equiv |\tilde{E}(\nu)|^2$ represents the smoothed envelope of the temporal power spectrum due to the 2-D SSD phase modulation ϕ_{2-D} SSD. The base-line 2-D SSD system yields $\Delta\nu_{\text{rss}} = 891$ THz and $\Delta\nu_{\text{eff}} = 979$ THz in the UV.

The bandwidth $\Delta\lambda_M$, laser divergence $\Delta\theta_M$ and the number of color cycles N_{cc} determine the required grating dispersion ξ , the temporal delay τ_D , modulator frequency ν_M , and modula-

tion depth δ_M for the given beam diameter D_{NIF} . Due to current pinhole requirements of the spatial filters, the imposed laser divergence is limited to $\Delta\theta_{M1} = 100$ μrad and $\Delta\theta_{M2} = 50$ μrad in the first and second dimensions, respectively. The number of color cycles across the beam is defined by $N_{\text{cc}} \equiv \tau_D\nu_M$, where τ_D is the time shear imposed by the dispersion gratings and ν_M is the modulator's frequency. It can be shown that the laser divergence $\Delta\theta_M$ is proportional to the applied SSD bandwidth $\Delta\lambda_M$ and is given by

$$\Delta\theta_M = \tau_D \Delta\lambda_M \frac{c}{\lambda_{IR} D_{NIF}}, \quad (10)$$

where c is the vacuum speed of light, $\lambda_{IR} = 1053$ nm is the IR vacuum wavelength, and $D_{NIF} = 35.1$ cm is the nominal beam diameter. Since the pinholes restrict the laser divergence $\Delta\theta_M$, and the base-line 2-D SSD design calls for $\Delta\lambda_{M1} = 10.8$ Å, applying Eq. (10) to the first dimension yields a time delay $\tau_{D1} = 114.15$ ps, which implies that the required modulator frequency for the first dimension, to achieve $N_{\text{cc}1} = 1$, is $\nu_{M1} = 8.76$ GHz. Similarly, applying Eq. (10) to the second dimension yields $\tau_{D2} = 309.60$ ps and $\nu_{M2} = 3.23$ GHz for $N_{\text{cc}2} = 1$. This base-line design will be designated as BL1 in this article. An alternative base-line 2-D SSD design, designated as BL2, is also proposed, which has $N_{\text{cc}1} = 2$, $\delta_{M1} = 8.33$, and $\nu_{M1} = 17.52$ GHz with all other parameters left the same. In addition, a base-line design the same as BL1 but without the temporal shear will be designated as BL1b. The relevant parameters are summarized in Table 86.III.

Ultrafast-Picket-Smoothing Scheme

The ultrafast-picket-smoothing scheme produces a sub-apertured near field that sweeps across the full-beam aperture when using a pulse-modulated laser whose pulse width is smaller than the residual time shear τ_{D1} due to the dispersing grating. The sweeping motion causes smoothing in the time-integrated far field because the speckle pattern changes as the sub-apertured near field moves across the randomly phased background of the DPP. Applying a time-varying phase or phase chirp to each picket enhances the efficiency of this smoothing mechanism. The phase chirp increases the inherent bandwidth of each pulse and asymptotically produces many independent speckle patterns (or far-field modes), similar to SSD, as long as the grating dispersion matches the pulse repetition rate. Unlike SSD, the phase chirp can be tailored to produce a uniform far-field distribution of modes that not only reduces the asymptotic nonuniformity but also alleviates pinhole loading in the laser amplification chain. The ultrafast-picket-smoothing scheme supplants only the first SSD

dimension. The efficient and asymptotic smoothing of the ultrafast pickets depends on a second and orthogonal SSD smoothing dimension in the same way that 2-D SSD does.

The ultrafast-picket-pulse train is defined to have an intensity FWHM pulse width of Δt_{FWHM} , a pulse repetition period of ΔT , and an inverse duty cycle given by $\text{IDC} \equiv \Delta T/\Delta t$, where Δt is the pulse width that contains 99% of the pulses's energy. The pulse train that will be discussed is a fourth-order super-Gaussian and can be written as

$$\text{picket}(t) \equiv \sum_{n=0}^N \exp \left[-\ln(2) \left(\frac{t-t_0-n\Delta T}{\Delta t_{\text{FWHM}}} \right)^4 \right], \quad (11)$$

s.t. $N\Delta T \leq 3$ ns. The pulse width as defined in Eq. (11) is $\Delta t = 28.1$ ps. The fundamental beam shape for the pickets is defined to be the same as the base-line 2-D SSD [i.e., Eq. (5)].

A pulsed laser beam followed by a phase modulator that is then dispersed by a grating describes any ultrafast-picket scheme schematically (see Fig. 86.41). This schematic graphically describes the mathematical functions of the resultant pulsed beam used in the *Waasikwa'* simulations. The phase modulator in Fig. 86.41 represents an optional phase chirp that can be applied to the pickets. If the phase chirp is locked to the pulse repetition rate of the pickets, the phase chirp of each picket, whose function is given by $\phi_{\text{chirp}}(t)$, is then appended to Eq. (11) in the form of $\exp[i\phi_{\text{chirp}}(t-t_0-n\Delta T)]$.

The grating G2, in Fig. 86.41, disperses the ultrafast pickets with a grating dispersion, ξ_y , which temporally shears the beam by an amount τ_{D1} . Consequently, the beam becomes sub-apertured and then sweeps across the whole near-field aperture as time progresses (see Fig. 86.42). The sub-apertured width

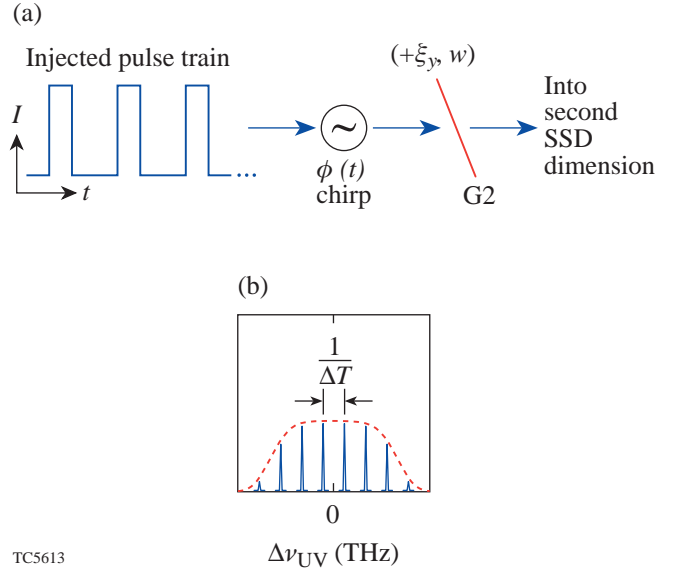


Figure 86.41 (a) Schematic describing a chirped UV pulsed beam in the *Waasikwa'* simulations. A pulse-modulated laser is chirped by the phase modulator M₁ with the phase given by $\phi_{\text{chirp}}(t)$ and then dispersed by the grating G2. This schematic does not describe the layout of an actual implementation; it is simply a graphical representation of the mathematical function of the resultant pulsed beam. (b) A plot representing the envelope of the temporal spectrum from a generic chirped-pulse train, which is identical to the temporal spectrum from a single chirped pulse. The series of delta functions represents the temporal-spectral modes from the chirped-pulse train that are spaced by $1/\Delta T$. The envelope modulates these modes.

W_a is equivalent to the ratio of the pulse width Δt to the grating dispersion ξ_y , which can then be related to other quantities,

$$W_a = \frac{\Delta t}{\xi_y} = \frac{\Delta T}{\xi_y \text{IDC}} = \frac{D_{\text{NIF}}}{\text{IDC} \cdot N'_{\text{cc}}}, \quad (12)$$

Table 86.III: Summary of the relevant parameters for the NIF 2-D SSD base-line models.

Sim Name	2-D SSD Base-Line Models													
	First Applied SSD Dimension						Second Applied SSD Dimension						Combined BW	
	δ_{M1}	ν_{M1} (GHz)	$\Delta\lambda_{M1}$ (Å) IR	$\Delta\nu_{M1}$ (GHz) UV	$\Delta\nu_{\text{eff}}$ (GHz) UV	$N_{\text{cc}1}$	δ_{M2}	ν_{M2} (GHz)	$\Delta\lambda_{M2}$ (Å) IR	$\Delta\nu_{M2}$ (GHz) UV	$\Delta\nu_{\text{eff}2}$ (GHz) UV	$N_{\text{cc}2}$	$\Delta\nu_{\text{rss}}$ (GHz)	$\Delta\nu_{\text{eff}}$ (GHz)
BL1	16.67	8.76	10.8	876	665	1	8.37	3.23	2.0	162	167	1	891	979
BL1b	16.67	8.76	10.8	876	665	1							891	979
BL2	8.333	17.52	10.8	876	656	2							891	979

where N'_{cc} is analogous to the number of color cycles in an SSD system and is defined as

$$N'_{cc} \equiv \frac{\tau_D}{\Delta T}. \tag{13}$$

When the quantity $N'_{cc} > 1$, multiple pickets will simultaneously illuminate the near field and will result in improved low-spatial-frequency smoothing and resonant features in the far-field power spectrum similar to an SSD system of multiple color cycles. The target will experience an intensity ripple when N'_{cc} is not an integer. Under these conditions, however, the IDC decreases, which degrades the benefit of improved frequency conversion and decreased power imbalance. When the quantity $N'_{cc} < 1$, the IDC increases (for a given grating dispersion) and will increase frequency conversion and reduce power imbalance. The target will experience an intensity ripple, however, due to the absence of any pickets over the duration of $\Delta T - \tau_D$ (unless the pickets can be timed to alter-

nately illuminate different beams in each quad to compensate). More importantly, the smoothing will become inefficient because the far-field modes will become statistically dependent, just as in the SSD case. When the quantity $N'_{cc} = 1$, the target will experience little ripple (in fact, if the pulse is rectangular, the target will experience no intensity ripple) and the smoothing will be efficient over all spatial wavelengths.

As originally conceived, the chirp would be applied by allowing the pickets to enter a phase-locked phase modulator such as the current fiber modulator. In this scenario the pulse period is phase-locked to the phase modulator such that the maximum instantaneous wavelength shift is applied to each picket (see Fig. 86.43). The pickets effectively “sample” the central portion of the bandwidth produced by the phase modulator. Notice in Fig. 86.43 how the “sampled” spectrum of the ultrafast pickets is nearly uniform and centrally distributed, unlike the distinctive Bessel mode pattern produced by the frequency-modulated (FM) spectrum of SSD.

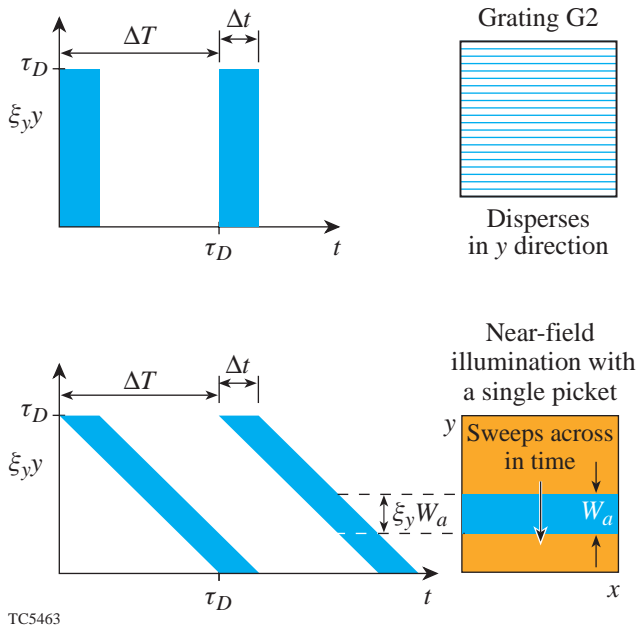


Figure 86.42 The two plots on the left-hand side represent beam cross sections before and after the grating G2, which temporally skews the beam. Consequently, the beam becomes sub-apertured and then sweeps across the whole near-field aperture as time progresses (see the plot on the lower right-hand side). If the pulse period Δt is chosen to equal the temporal shear τ_D from grating G2, the target will be continuously illuminated since as one picket exits the aperture, the next one will enter on the opposite side.

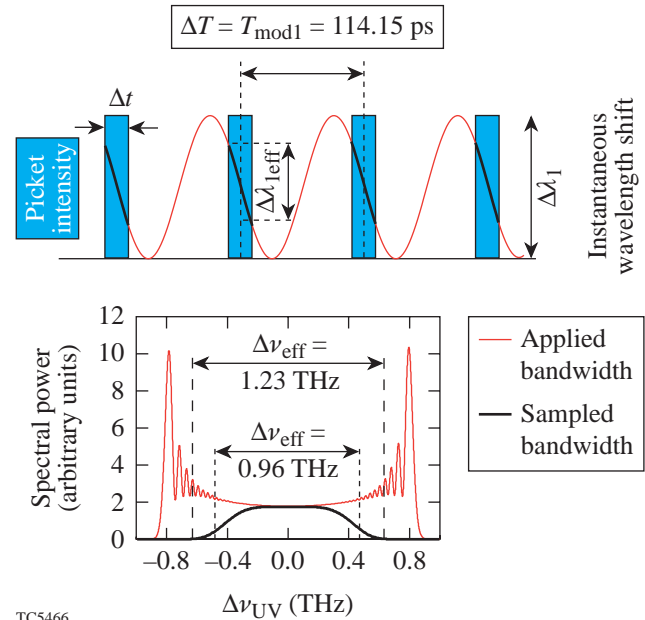


Figure 86.43 A chirp is applied to each picket using a phase-locked modulator. This diagram graphically illustrates how the modulator applies the maximum instantaneous wavelength shift to each picket. The pickets effectively “sample” the central portion of the bandwidth applied by the modulator.

1. Temporal Spectrum and Diffraction-Limited Far-Field Pattern of Ultrafast Pickets

The centrally distributed sampled spectrum directly translates into reduced pinhole loading. The applied temporal spectrum maps into the pattern of a diffraction-limited far field since the dispersed beam maps the applied temporal bandwidth into spatial bandwidth (see Ref. 16 for a detailed description). The time-integrated, diffraction-limited far-field patterns of the NIF 2-D SSD base-line and ultrafast pickets are illustrated in Fig. 86.44. The pattern from the NIF 2-D SSD base line

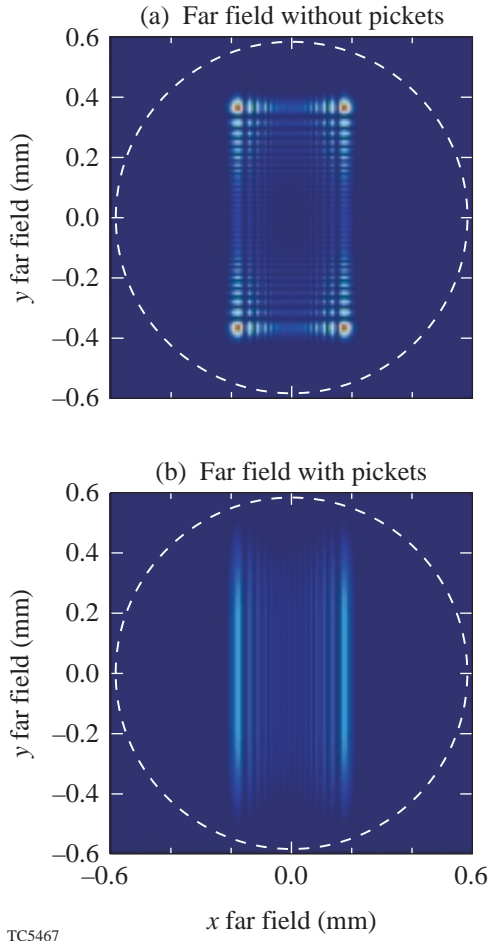


Figure 86.44

The time-integrated diffraction-limited far-field patterns for the NIF 2-D SSD (a) base-line and (b) ultrafast pickets. The images are plotted using the same gray scale to indicate relative fluence levels. The pattern from the NIF 2-D SSD base line shows high fluence levels near the four outer corners of the pattern. In contrast, the pattern from the ultrafast-picket design shows a much lower, uniform fluence level more evenly distributed about the center. Both images show the distinct Bessel pattern in the direction corresponding to the second SSD dimension.

[Fig. 86.44(a)] shows high fluence levels near the four outer corners of the pattern. In contrast, the pattern from the ultrafast-picket design [Fig. 86.44(b)] shows a much lower and uniform fluence level more evenly distributed about the center. Both images show the distinct Bessel mode pattern in the direction corresponding to the second SSD dimension.

The temporal spectral modes of the ultrafast picket fence are separated by the inverse of the pulse repetition period, e.g., $1/\Delta T$, and they conform to the envelope of the spectrum of a single pulse [see Fig. 86.41(b)]. These spectral modes become modes in the far field and lead to the number of independent speckle patterns in the asymptotic limit. The mode spacing in the far field in the direction corresponding to the grating G2 is calculated by $N'_{cc} f_{NIF} \lambda_{UV} / D_{NIF}$. The number of modes due to the ultrafast pickets can be calculated using

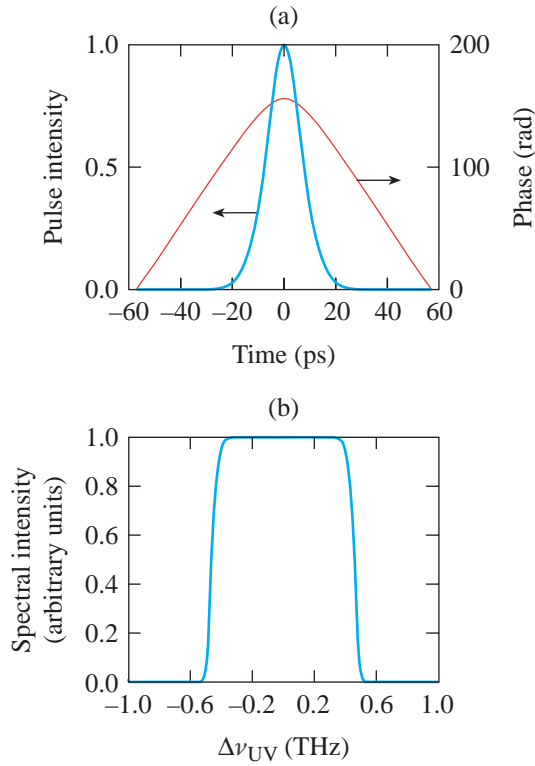
$$\text{Modes}' = \Delta v'_{UV} \cdot \Delta T = \frac{\Delta \theta'_{M1}}{\xi_y \lambda_{UV}} \Delta T = \frac{\Delta \theta'_{M1} D_{NIF}}{\lambda_{UV} N'_{cc}}. \quad (14)$$

The number of modes due to the SSD for either dimension can be calculated using

$$\text{Modes} = \frac{\Delta v_{UV}}{v_M} = \frac{\Delta \theta_M D_{NIF}}{\lambda_{UV} N_{cc}}, \quad (15)$$

where the laser divergence $\Delta \theta_M$ and number of color cycles N_{cc} corresponding to either SSD dimension is substituted into Eq. (15). The total number of modes in the far field is computed as the product of the number of modes from the first smoothing dimension (either SSD or ultrafast picket fence) and the number due to the second orthogonal SSD dimension. If the temporal spectrum of either the ultrafast pickets or SSD is nonuniform, the effective number of modes is reduced, similar to SSD.¹⁸ The reduction ratio is approximated as the ratio of the effective bandwidth calculated using Eq. (9) to the overall bandwidth of each smoothing direction separately. The ultrafast-picket-fence schemes proposed in this article have a very uniform distribution, which can decrease the asymptotic level reached by approximately 20% as compared to base-line 2-D SSD.

The temporal spectrum of the ultrafast pickets can be modified or tailored to reduce the pinhole loading due to the tails of the spectrum seen in Fig. 86.43. Through an iterative Fourier technique, similar to phase-retrieval techniques, a chirped pulse can be designed to produce the high-order super-Gaussian temporal spectrum as illustrated in Fig. 86.45.



TC5594

Figure 86.45

A chirped pulse (a) and its temporal spectrum (b). The spectrum was the design point of an iterative Fourier technique to find the required shape and phase of the pulse in (a). This spectrum can further reduce the pinhole loading by removing the energy located in the tails of the spectrum seen in Fig. 86.43.

2. Alternate Methods of Producing Chirped Ultrafast Pickets

Alternate methods are available for producing chirped ultrafast pickets that need not be phase locked. One method is to reflect a stretched and longer chirped pulse from a fiber-Bragg grating; this results in a train of chirped pulses of desired shape and chirp by properly engineering the fiber. This technique meshes well with the tailored chirped pulse seen in Fig. 86.45 since the pulse shape is approximately a $\text{sec } h^2$ and the chirp is nearly linear, both of which are easily obtained using current laser and fiber technologies.

Far-Field Simulation and Analysis

Waasikwa' calculates the planar far-field fluence using

$$F(x_{\text{ff}}, y_{\text{ff}}) \equiv \int_{\text{pulse duration}} I_{\text{ff}}(x_{\text{ff}}, y_{\text{ff}}, t) dt, \quad (16)$$

where $I_{\text{ff}}(x_{\text{ff}}, y_{\text{ff}}, t)$ represents the instantaneous far-field intensity. The evolution of the far-field intensity is calculated by taking the modulus squared of a 2-D spatial Fourier transform of the UV near field [comp. Ref. 19, pp. 83–89]:

$$I_{\text{ff}}(x_{\text{ff}}, y_{\text{ff}}, t) \equiv \left| \iint_{\forall \text{space}} E(x, y, t) \exp \left[-i \frac{2\pi}{\lambda_{\text{UV}} f_{\text{NIF}}} (x_{\text{ff}} x + y_{\text{ff}} y) \right] dx dy \right|^2, \quad (17)$$

where $E(x, y, t)$ represents the complex-valued UV electric field strength in the near field and (x, y) and $(x_{\text{ff}}, y_{\text{ff}})$ are the near- and far-field coordinate systems, respectively; $\lambda_{\text{UV}} = 351$ nm is the UV vacuum wavelength; and $f_{\text{NIF}} = 770$ cm is the assumed NIF focal length. The integrations are calculated as a running summation at every simulation time step dt . For these ~ 1 -THz-bandwidth pulsed beams, the time step is defined to be $dt = 0.75$ ps, which sufficiently over-samples the bandwidth based on the Nyquist criterion.

The 2-D power spectral density (2-D power spectrum or simply the 2-D PSD) is derived from the simulated far-field fluence by taking the modulus squared of the 2-D spatial Fourier transform:

$$\text{PSD}(k_{x_{\text{ff}}}, k_{y_{\text{ff}}}) \equiv \left| \iint_{\forall \text{far field}} F(x_{\text{ff}}, y_{\text{ff}}) \exp \left[-i(k_{x_{\text{ff}}} x_{\text{ff}} + k_{y_{\text{ff}}} y_{\text{ff}}) \right] dx_{\text{ff}} dy_{\text{ff}} \right|^2, \quad (18)$$

where $F(x_{\text{ff}}, y_{\text{ff}})$ represents the far-field fluence as defined by Eq. (16), $(x_{\text{ff}}, y_{\text{ff}})$ is the far-field coordinate system, and $(k_{x_{\text{ff}}}, k_{y_{\text{ff}}})$ is the far-field's spatial-frequency coordinate system. The azimuthal sum at each radial wave number of the 2-D power spectrum defines the 1-D power spectral density (1-D power spectrum or simply the 1-D PSD) and is given by

$$\text{psd}(k_{\text{ff}}) \equiv \oint \text{PSD}(k_{x_{\text{ff}}}, k_{y_{\text{ff}}}) k_{\text{ff}} d\theta, \quad (19)$$

where the transformation into polar coordinates is defined as $k_{\text{ff}} \equiv \sqrt{k_{x_{\text{ff}}}^2 + k_{y_{\text{ff}}}^2}$ and $\tan \theta \equiv k_{y_{\text{ff}}} / k_{x_{\text{ff}}}$. The single-beam

irradiation nonuniformity σ_{rms} is defined as the square root of the ratio of the speckle power (e.g., the high frequencies $k_{\text{ff}} \geq 5.88$ rad/mm at the NIF target plane or ℓ -modes $\ell \geq 10$) to the envelope power of the far-field spot (i.e., the low frequencies $k_{\text{ff}} < 5.88$ rad/mm). The wave number 5.88 rad/mm divides the envelope and speckle frequencies. A finite entrance pupil imposes a limitation on the spatial-frequency bandwidth of an optical system (compare the intensity-impulse response or point-spread function of a diffraction-limited system with a rectangular exit-pupil function in Ref. 19, pp. 110–113). On the NIF, the highest spatial frequency of the far field, regardless of the near-field beam profile, is limited by the finite square shape of the full aperture beam whose width is defined as $D_{\text{NIF}} = 35.1$ cm. Consequently, the 2-D PSD possesses a square-shaped absolute cutoff whose width along both the $k_{x\text{ff}}$ and $k_{y\text{ff}}$ axes corresponds to the f -number limited spatial frequency

$$k_{\text{cutff}} = \frac{2\pi D_{\text{NIF}}}{\lambda_{\text{UV}} f_{\text{NIF}}} = 0.816 \frac{\text{rad}}{\mu\text{m}}. \quad (20)$$

Due to the square-shaped cutoff of the 2-D PSD, the 1-D PSD has an absolute cutoff of

$$k'_{\text{cutff}} = \sqrt{2} \cdot k_{\text{cutff}}. \quad (21)$$

For the ultrafast picket fence schemes, the high aspect ratio (which is proportional to IDC) of the sub-apertured near field corresponds to an absolute cutoff $k'_{\text{cutff}} \cong k_{\text{cutff}}$.

Smoothing Performance Results

Waasikwa' far-field simulations calculated the single-beam nonuniformity as a function of time for a duration of 3 ns. Three NIF 2-D SSD base-line designs and four ultrafast picket designs were calculated using the parameters listed in Tables 86.III and 86.IV. The names listed under the ‘‘Sim Name’’ column in these tables will be used to designate each model.

The smoothing performances for Picket1, Picket2, and the BL1 designs are plotted in Fig. 86.46 for a 3-ns duration for all

Table 86.IV: Summary of the relevant parameters for the NIF ultrafast-picket-smoothing schemes. The second SSD dimension has the same parameters as in Table 86.III.

Sim Name	Pulse Type	First Smoothing Dimension										Combined BW
		Applied SSD				Ultrafast Pickets						
		δ_{M1}	ν_{M1} (GHz)	$\delta\lambda_{\text{M1}}$ (Å) IR	N_{cc1}	IDC	N'_{cc}	ΔT (ps)	Δt_{FWHM} (ps)	Δt (ps)	$\Delta\nu_{\text{eff}}$ (GHz) UV	
Picket1	Single SG4	31.02	8.76	20.1	1	4	1	114.15	19.0	28.1	970	994
Picket1b	Single SG4	31.02	8.76	20.1	1	4	1	114.15	19.0	28.1	970	994
Picket2	Double SG4	31.02	8.76	20.1	1	2	2	57.075	19.0	28.1	970	995
Chirped1	Single sech^2	n/a	n/a	n/a	n/a	2.5	1	114.15	19.0	45	947	993

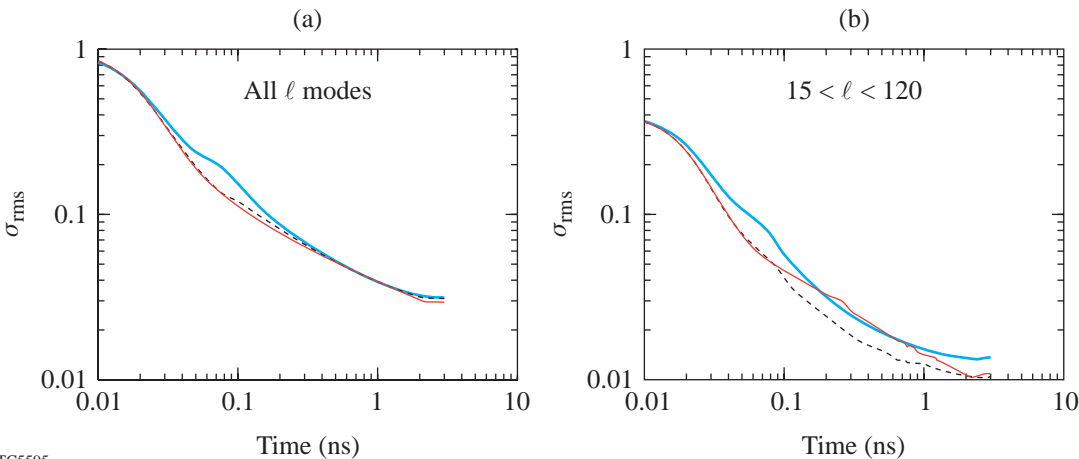


Figure 86.46 The nonuniformity plotted against time for (a) all ℓ modes and (b) the ℓ -mode range $15 < \ell < 120$. The red line is the NIF ultrafast Picket1, the dashed line is the NIF ultrafast Picket2, and the blue line is the NIF 2-D SSD base-line BL1.

TC5595

the ℓ modes and over the ℓ -mode range of $15 < \ell < 120$. The smoothing performance of both picket designs is initially better than and later is nearly equivalent to BL1 design. The Picket2 design produces better smoothing than the other two designs for the range $15 < \ell < 120$ because two pickets are simultaneously illuminated, which is analogous to a two-color-cycle 2-D SSD system. The smoothing performances for the tailored chirped pulse (designated as Chirped1), Picket1, and BL1 are plotted in Fig. 86.47 for a 3-ns duration for all the ℓ -modes and over the ℓ -mode range, $15 < \ell < 120$.

The smoothing performances for the BL1, Picket1, and Picket2 simulations are identical for the first 15 ps because they have the same pulse rise time and a similarly shaped sub-apertured near field (BL1 is sub-apertured during the time corresponding to the initial temporal shear and the shape matches the picket's shape for the first 15 ps). The smoothing performance for Chirped1 is initially not as good as Picket1 or Picket2 because it has a much longer rise time of approximately 25 ps. The smoothing performance for both picket types, however, is better than BL1 over the duration 20 ps $< t < 200$ ps. This is due to the fact that the ultrafast picket designs are designed to smooth efficiently, i.e., full-smoothing, full-bandwidth for a sub-apertured near field; whereas the base-line designs do not achieve full-smoothing/full-bandwidth until the aperture is filled, i.e., after the initial temporal shear $\tau_{D1} = 114.15$ ps. Therefore, the picketed designs effectively have ~ 115 ps of smoothing accomplished before the base-line designs achieve efficient smoothing. Over the ℓ -band

range $20 \leq \ell < 120$, Picket2 has better smoothing performance than Picket1 for $t > 80$ ps because by this time the second picket has appeared in Picket2 and remains for the rest of the simulation. The second picket reduces the nonuniformity in this ℓ -band range due to the aforementioned multiple-color-cycle effects. The overall smoothing performance for all the simulations are nearly equivalent, for the duration $t > 200$ ps and until the asymptotic levels are reached (approximately $t \sim 3$ ns). The Picket #1 simulation has reduced asymptotic overall nonuniformity because of the uniform bandwidth distribution. The simulation Picket1 has a lower asymptotic nonuniformity relative to Picket2 because of $N'_{cc} = 2$. The asymptotic levels for both picket-type simulations, however, are nearly equivalent for the ℓ -band range $15 \leq \ell \leq 120$.

The instantaneous 1-D PSD, defined by Eq. (19), for the ultrafast-picket-fence schemes is approximately $4\times$ higher over the ℓ -band range $15 \leq \ell \leq 120$ as compared to BL1 (see Fig. 86.48). The ultrafast-picket-fence schemes produce a sub-apertured near field, which corresponds to a 2-D PSD whose extent (i.e., its cutoff wave number $k_{cut_{ff}}$) is reduced in the corresponding direction by a factor of $\sim IDC$ (for $N'_{cc} = 1$). By conservation of energy, the sub-apertured near field increases the spectral power in the picketed direction by a factor of $\sim IDC$. Consequently, the azimuthal sum (i.e., the 1-D PSD) reflects this additional power. Note also that there is still power up to $k_{cut_{ff}} = 0.816$ rad/ μm because the second SSD dimension is still full aperture.

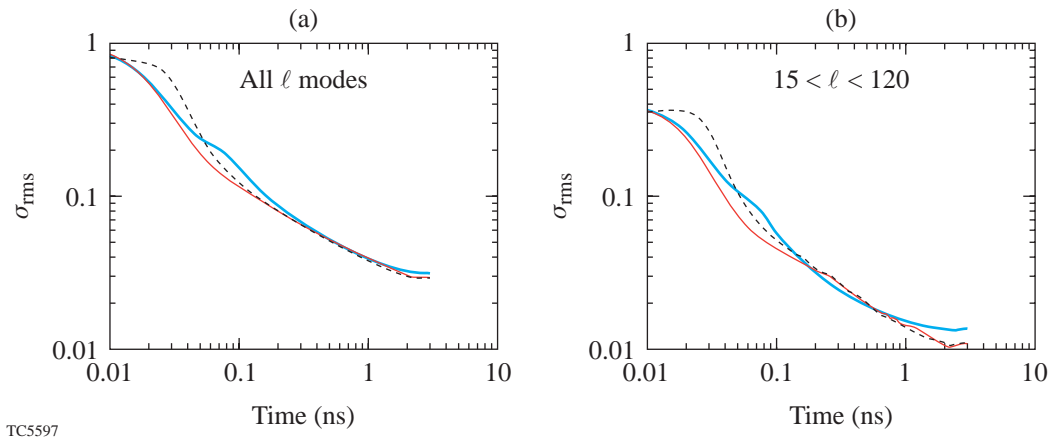


Figure 86.47 The nonuniformity plotted against time for (a) all ℓ modes and (b) the ℓ -mode range $15 < \ell < 120$. The red line is the NIF ultrafast Picket1, the dashed line is the NIF ultrafast chirped-picket Chirped1, and the blue line is the NIF 2-D SSD base-line BL1.

To relate the smoothing performance to effective bandwidth or inverse coherence time, the initial rise-time behavior must be eliminated because the simple model of the nonuniformity as a function of time and wave number does not account for this rise-time behavior⁷

$$\sigma^2(t, k_{\text{ff}}) = \sigma_0^2(k_{\text{ff}}) \frac{t_c}{t + t_c} + \sigma_{\text{asym}}^2(k_{\text{ff}}), \quad (22)$$

where $\sigma_0^2(k_{\text{ff}}) = \sigma^2(0, k_{\text{ff}})$ is the initial value of the nonuniformity and $\sigma_{\text{asym}}^2(k_{\text{ff}}) = \sigma^2(\infty, k_{\text{ff}})$ is the asymptotic level of the nonuniformity for the radial wave number k_{ff} . Advancing the pulse by this delay and delaying the time-integrated far field by the same time accomplish this task. Therefore, two additional simulations were run with a delay of an amount corresponding to the rise-time delay for each model. The base-line model BL1b is identical to BL1 except for the included delay of 130 ps. The ultrafast-picket-fence model Picket1b is identical to Picket1 except for the included delay of 30 ps.

The nonuniformity of Picket1b is nearly equivalent to BL1b over the ℓ -band range $15 \leq \ell \leq 120$ even though the instanta-

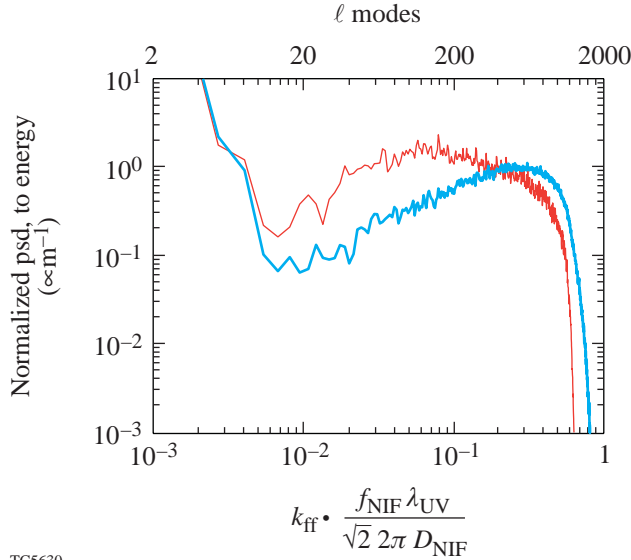


Figure 86.48

The instantaneous far-field 1-D power spectra for models BL1 (blue line) and Picket1 (red line). The subapertured near field of the ultrafast picket scheme increases the power in modes $\ell < 400$ relative to the base-line 2-D SSD model. The increase is approximately equal to the IDC value for the ultrafast picket scheme over the majority of the affected ℓ modes.

neous power is $4\times$ higher in these modes (see Fig. 86.48). The reason for this behavior is simple: the effective bandwidth or inverse coherence time is approximated $4\times$ higher for Picket1b relative to BL1b. The sub-apertured near field of the Picket1b causes the bandwidth to be distributed over a reduced wave-number range and consequently smoothes these wavelengths faster. This effect is calculated two independent ways: (1) smoothing performance of a full simulation is fit to the model of Eq. (22) and (2) a phenomenological model is developed.

Calculating the effective bandwidth distribution for either the 2-D SSD system or the ultrafast-picket-fence scheme is essentially a 2-D problem. Two- and one-dimensional phenomenological models of the effective bandwidth are given here. In the first smoothing direction, the bandwidth is distributed as¹⁰

$$\Delta v_x(k_{x_{\text{ff}}}) = 2\Delta v_{M1} \sin\left(k_{x_{\text{ff}}} \frac{\kappa_1}{2} N_{\text{cc1}}\right), \quad (23)$$

where Δv_{M1} is the FM modulator bandwidth in the UV for the first SSD modulator or the chirped-pulse bandwidth and the parameter κ_1 is the one-half speckle width, ($\kappa_1 = \kappa_{\text{SSD1}} = f_{\text{NIF}}/\lambda_{\text{UV}}/D_{\text{NIF}}$ for the first SSD dimension or $\kappa_1 = \kappa_{\text{picket}} = \text{IDC} \cdot f_{\text{NIF}} \lambda_{\text{UV}}/D_{\text{NIF}}$ for the ultrafast picket fence). In the second smoothing direction, the bandwidth is distributed as

$$\Delta v_y(k_{y_{\text{ff}}}) = 2\Delta v_{M2} \sin\left(k_{y_{\text{ff}}} \frac{\kappa_2}{2} N_{\text{cc2}}\right), \quad (24)$$

where Δv_{M2} is the FM modulator bandwidth in the UV for the second SSD modulator and $\kappa_2 = \kappa_{\text{SSD1}}$ is the one-half speckle width for the second SSD dimension. For the 2-D problem, it is assumed that the orthogonal components of the wave vector $\mathbf{k}_{\text{ff}} \equiv k_{x_{\text{ff}}} \hat{x} + k_{y_{\text{ff}}} \hat{y}$ are affected independently so that the effective bandwidth is given by the quadrature sum

$$\Delta v'_{\text{eff}}(k_{x_{\text{ff}}}, k_{y_{\text{ff}}}) = \sqrt{|\Delta v_x(k_{x_{\text{ff}}})|^2 + |\Delta v_y(k_{y_{\text{ff}}})|^2}. \quad (25)$$

The smoothing of the 1-D PSD then corresponds to the weighted azimuthal average of the two-dimensional effective bandwidth function Eq. (25).

$$\Delta v_{\text{eff}}(k_{\text{ff}}) = \frac{\oint \Delta v'_{\text{eff}}(k_{x_{\text{ff}}}, k_{y_{\text{ff}}}) \text{PSD}_0(k_{x_{\text{ff}}}, k_{y_{\text{ff}}}) k_{\text{ff}} d\theta}{\oint \text{PSD}_0(k_{x_{\text{ff}}}, k_{y_{\text{ff}}}) k_{\text{ff}} d\theta}, \quad (26)$$

where the weighting function $\text{PSD}_0(k_{x\text{ff}}, k_{y\text{ff}})$ is the 2-D PSD of the aberration-free ideal near field of Eq. (4) at one instant of time for either the 2-D SSD base-line full-aperture designs or the sub-apertured ultrafast picket-fence designs.

The nonuniformity $\sigma^2(t, k_{\text{ff}})$ calculated from the simulations BL1b and Picket1b is fit to the nonuniformity model of Eq. (22) using the coherence time as the one degree of freedom in order to estimate the effective bandwidth by $\Delta\tilde{v}_{\text{eff}}(k_{\text{ff}}) = 1/t_c$. The simulation data $\sigma^2(t, k_{\text{ff}})$ is averaged over ± 5 neighboring wave numbers before being fit to the model of Eq. (22). The estimated effective bandwidth by $\Delta\tilde{v}_{\text{eff}}(k_{\text{ff}})$ is compared to that calculated with the phenomenological effective bandwidth model given by Eq. (26) [see Fig. 86.49(a)]. The ratio of the effective bandwidths from the phenomenological model is plotted in Fig. 86.49(b). The fact that the effective bandwidth for the Picket1b is approximately 4x higher than the BL1b over the ℓ -band range $15 \leq \ell \leq 120$ explains why they have a similar smoothing performance over the l-band range in Fig. 86.46(b).

Conclusion

The underlying motivation of implementing the ultrafast pickets on the NIF is the ability to increase the frequency-conversion efficiency and to reduce the contribution to the beam-to-beam power imbalance in the foot portion of an ICF laser pulse.⁵ In this article, the smoothing performance of the ultrafast pickets was analyzed and shown to be equivalent to the NIF 2-D SSD base-line designs for direct-drive ICF as long as the applied bandwidths and divergences are close to the base-line designs. If no bandwidth is applied in the first dimension or if the IDC is too large, the early-time smoothing performance is not as effective. It was also discovered that the diffraction-limited far-field pattern produced by the chirped pickets can reduce pinhole loading, which might lead to an increase in the permitted laser divergence. Overall, a properly designed ultrafast picket system offers many system-wide benefits at the cost of a more complicated front end.

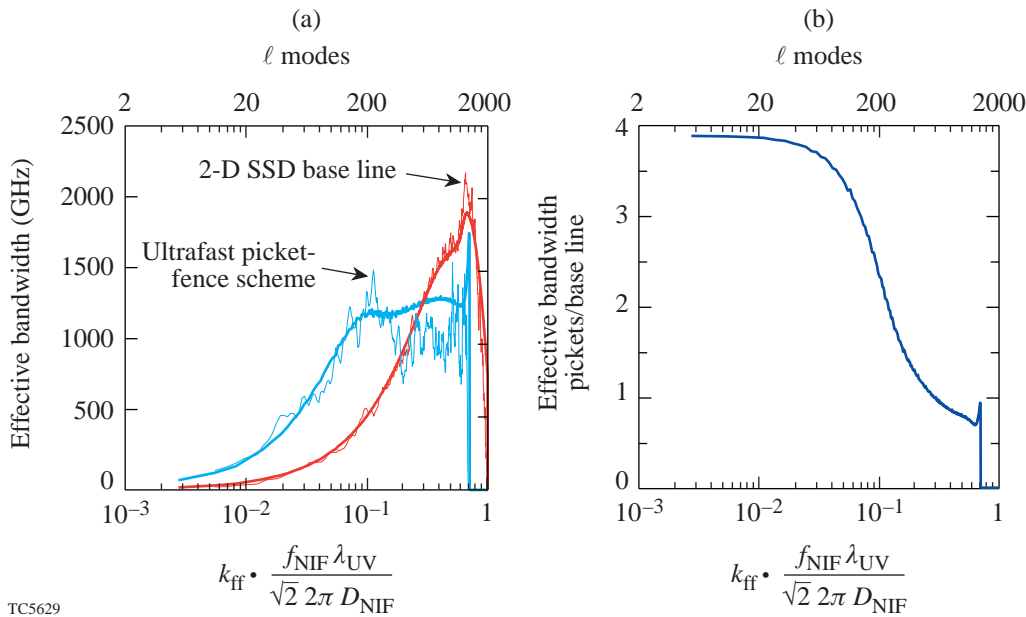


Figure 86.49

(a) The one-dimensional phenomenological model of the effective bandwidth $\Delta v_{\text{eff}}(k_{\text{ff}})$ and the estimated effective $\Delta\tilde{v}_{\text{eff}}(k_{\text{ff}})$ bandwidth are compared for both the BL1b and Picket1b *Waasikwa*' simulations. The bold traces represent the phenomenological model $\Delta v_{\text{eff}}(k_{\text{ff}})$, and the thin traces represent the simulation's effective bandwidth $\Delta\tilde{v}_{\text{eff}}(k_{\text{ff}})$. (b) The ratio of phenomenological models $\Delta v_{\text{eff}}(k_{\text{ff}})$ for Picket1b to BL1b is plotted, which shows the increased bandwidth in the lower ℓ -band range.

ACKNOWLEDGMENT

This work was partially supported by the U.S. Department of Energy Office of Inertial Confinement Fusion under Cooperative Agreement No. DE-FC03-92SF19460, the University of Rochester, and the New York State Energy Research and Development Authority. The support of DOE does not constitute an endorsement by DOE of the views expressed in this article.

REFERENCES

1. C. P. Verdon, *Bull. Am. Phys. Soc.* **38**, 2010 (1993).
2. S. E. Bodner, D. G. Colombant, J. H. Gardner, R. H. Lehmborg, S. P. Obenschain, L. Phillips, A. J. Schmitt, J. D. Sethian, R. L. McCrory, W. Seka, C. P. Verdon, J. P. Knauer, B. B. Afeyan, and H. T. Powell, *Phys. Plasmas* **5**, 1901 (1998).
3. D. K. Bradley, J. A. Delettrez, and C. P. Verdon, *Phys. Rev. Lett.* **68**, 2774 (1992); J. Delettrez, D. K. Bradley, and C. P. Verdon, *Phys. Plasmas* **1**, 2342 (1994); J. D. Kilkenny, S. G. Glendinning, S. W. Haan, B. A. Hammel, J. D. Lindl, D. Munro, B. A. Remington, S. V. Weber, J. P. Knauer, and C. P. Verdon, *Phys. Plasmas* **1**, 1379 (1994); R. Epstein, *J. Appl. Phys.* **82**, 2123 (1997); V. A. Smalyuk, T. R. Boehly, D. K. Bradley, V. N. Goncharov, J. A. Delettrez, J. P. Knauer, D. D. Meyerhofer, D. Oron, and D. Shvarts, *Phys. Rev. Lett.* **81**, 5342 (1998).
4. F. J. Marshall and G. R. Bennett, *Rev. Sci. Instrum.* **70**, 617 (1999); F. J. Marshall, J. A. Delettrez, V. Yu. Glebov, R. P. J. Town, B. Yaakobi, R. L. Kremens, and M. Cable, *Phys. Plasmas* **7**, 1006 (2000).
5. J. E. Rothenberg, *Appl. Opt.* **39**, 6931 (2000).
6. T. R. Boehly, D. L. Brown, R. S. Craxton, R. L. Keck, J. P. Knauer, J. H. Kelly, T. J. Kessler, S. A. Kumpan, S. J. Loucks, S. A. Letzring, F. J. Marshall, R. L. McCrory, S. F. B. Morse, W. Seka, J. M. Soures, and C. P. Verdon, *Opt. Commun.* **133**, 495 (1997).
7. S. P. Regan, J. A. Marozas, J. H. Kelly, T. R. Boehly, W. R. Donaldson, P. A. Jaanimagi, R. L. Keck, T. J. Kessler, D. D. Meyerhofer, W. Seka, S. Skupsky, and V. A. Smalyuk, *J. Opt. Soc. Am. B* **17**, 1483 (2000).
8. S. Skupsky, R. W. Short, T. Kessler, R. S. Craxton, S. Letzring, and J. M. Soures, *J. Appl. Phys.* **66**, 3456 (1989).
9. Laboratory for Laser Energetics LLE Review **69**, 1, NTIS document No. DOE/SF/19460-152 (1996) (copies may be obtained from the National Technical Information Service, Springfield, VA 22161); S. Skupsky and R. S. Craxton, *Phys. Plasmas* **6**, 2157 (1999).
10. J. E. Rothenberg, *J. Opt. Soc. Am. B* **14**, 1664 (1997).
11. T. J. Kessler, Y. Lin, J. J. Armstrong, and B. Velazquez, in *Laser Coherence Control: Technology and Applications*, edited by H. T. Powell and T. J. Kessler (SPIE, Bellingham, WA, 1993), Vol. 1870, pp. 95–104.
12. Y. Lin, T. J. Kessler, and G. N. Lawrence, *Opt. Lett.* **21**, 1703 (1996).
13. Y. Kato, unpublished notes from work at LLE, 1984; K. Tsubakimoto *et al.*, *Opt. Commun.* **91**, 9 (1992); K. Tsubakimoto *et al.*, *Opt. Commun.* **103**, 185 (1993).
14. Laboratory for Laser Energetics LLE Review **45**, 1, NTIS document No. DOE/DP40200-149 (1990) (copies may be obtained from the National Technical Information Service, Springfield, VA 22161); T. E. Gunderman, J.-C. Lee, T. J. Kessler, S. D. Jacobs, D. J. Smith, and S. Skupsky, in *Conference on Lasers and Electro-Optics*, Vol. 7, 1990 OSA Technical Digest Series (Optical Society of America, Washington, DC, 1990), p. 354.
15. J. A. Marozas, S. P. Regan, J. H. Kelly, D. D. Meyerhofer, W. Seka, and S. Skupsky, "Laser Beam Smoothing Caused by the Small-Spatial-Scale *B*-Integral," to be published in the *Journal of the Optical Society of America B*.
16. Laboratory for Laser Energetics LLE Review **78**, 62, NTIS document No. DOE/SF/19460-295 (1999). Copies may be obtained from the National Technical Information Service, Springfield, VA 22161.
17. R. N. Bracewell, *The Fourier Transform and Its Applications*, 2nd ed., rev., McGraw-Hill Series in Electrical Engineering. Circuits and Systems (McGraw-Hill, New York, 1986).
18. J. E. Rothenberg, in *Solid State Lasers for Application to Inertial Confinement Fusion*, edited by W. F. Krupke (SPIE, Bellingham, WA, 1995), Vol. 2633, pp. 634–644.
19. J. W. Goodman, *Introduction to Fourier Optics* (McGraw-Hill, New York, 1968).